

RESEARCH ARTICLE | MAY 06 2025

## Nonlinear evolution and energy dissipation in shear-driven collisionless plasma turbulence

J. Goodwill ; S. Adhikari ; X. Li ; F. Pucci ; Y. Yang ; F. Guo ; W. H. Matthaeus 



*Phys. Plasmas* 32, 052301 (2025)

<https://doi.org/10.1063/5.0255087>



### Articles You May Be Interested In

Comparative simulations of Kelvin–Helmholtz induced magnetic reconnection at the Earth's magnetospheric flanks

*Phys. Plasmas* (May 2024)



Physics of Plasmas

## Special Topics Open for Submissions

[Learn More](#)

# Nonlinear evolution and energy dissipation in shear-driven collisionless plasma turbulence

Cite as: Phys. Plasmas **32**, 052301 (2025); doi: [10.1063/5.0255087](https://doi.org/10.1063/5.0255087)

Submitted: 26 December 2024 · Accepted: 12 April 2025 ·

Published Online: 6 May 2025



View Online



Export Citation



CrossMark

J. Goodwill,<sup>1,a)</sup> S. Adhikari,<sup>1</sup> X. Li,<sup>2</sup> F. Pucci,<sup>3</sup> Y. Yang,<sup>1</sup> F. Guo,<sup>2</sup> and W. H. Matthaeus<sup>1</sup>

## AFFILIATIONS

<sup>1</sup>Department of Physics and Astronomy, University of Delaware, Newark, Delaware 19716, USA

<sup>2</sup>Los Alamos National Laboratory, Los Alamos, New Mexico 87545, USA

<sup>3</sup>National Research Council, Institute for Plasma Science and Technology (CNR-ISTP), Bari 70125, Italy

<sup>a)</sup>Author to whom correspondence should be addressed: [goodwill@udel.edu](mailto:goodwill@udel.edu)

## ABSTRACT

Turbulence is often driven by velocity shears or temperature gradients. Previous studies have emphasized shear-driven plasma dynamics initiated by linear (Kelvin–Helmholtz) instability and leading to saturation due to vortex roll-up. For the collisionless plasma case, small-scale kinetic effects responsible for energy conversion and dissipation have been studied in fully developed turbulence and in magnetic reconnection; here, this analysis is applied to velocity shear-driven turbulence using particle-in-cell simulations. An emphasis is on the description of evolving turbulent characteristics in relation to dissipation and coherent structures. The results quantify partitioning between electron and proton heating as well as the spatial intermittency of dissipation for each species. The results may be relevant to interpretation of Magnetosphere Multiscale mission data and Parker Solar Probe measurements in regions where unequal proton–electron heating as well as shear-driven turbulence may be present.

© 2025 Author(s). All article content, except where otherwise noted, is licensed under a Creative Commons Attribution (CC BY) license (<https://creativecommons.org/licenses/by/4.0/>). <https://doi.org/10.1063/5.0255087>

## I. INTRODUCTION

Turbulence is frequently driven by gradients, often in the form of velocity shears or temperature gradients. These are familiar circumstances in hydrodynamics, and also in magnetohydrodynamic (MHD) treatments of plasmas.<sup>1</sup> In space and astrophysical plasmas in particular, velocity shear-driven turbulence, as well as related instabilities, lead to enhanced turbulence,<sup>2</sup> modifications to transport, and resulting turbulent heating.<sup>3</sup> Much of the attention to shear-driven plasma dynamics has concentrated on initiation of the process through linear (Kelvin–Helmholtz) instability<sup>4–6</sup> or its large-scale effects when reaching saturation due to vortex roll-up.<sup>7,8</sup> These have been most completely studied for collisional MHD plasmas where pressure is isotropic and dissipation is controlled by viscosity and resistivity. For collisionless plasma, the corresponding small-scale kinetic effects responsible for energy conversion and dissipation have been studied in fully developed Alfvénic turbulence, with near-equipartitioned velocity and magnetic fluctuation energies, and in magnetic reconnection systems.<sup>9–13</sup> A major goal of the present paper is to apply these analysis methods from initiation of a velocity shear-driven collisionless plasma into fully developed turbulence.

The classical picture of turbulence proposes that the energy cascade is caused by nonlinear interactions that transport energy from large-scale fluctuations down to small scales until ultimately dissipation occurs.<sup>14–16</sup> The MHD approach to the study of solar wind turbulence has shown promise in describing this energy cascade and the predictions based on MHD have been confirmed with data from numerous space missions.<sup>17–19</sup> However, it has become clear that a simplified MHD fluid model must be updated to include kinetic processes [reconnection, kinetic Alfvén waves (KAWs), etc.] that alter the energy cascade, and account for the heating that generates large-scale flows such as the solar wind itself.<sup>20</sup> Furthermore, numerous aspects of fully developed classical turbulence theory are based on the assumption of locality in scale of energy transfer, an idea that may be questioned for magnetized plasmas.<sup>19,21</sup>

This paper aims to expand on these questions by examining numerical simulation of turbulent dynamics emerging from an initially laminar flow in a collisionless medium. Beginning with initiation of dynamics by a large-scale shear layer of initial thickness  $2d_i$ , we study the time evolution of turbulence characteristics such as energy spectra, local energy enhancements, and preferential heating related to

coherent structures. Ultimately, the system displays features similar to findings from more homogeneous plasma simulations, as well as solar wind observations. Furthermore, understanding the spatial structure of energy dissipation in this system may provide insight for regarding observational analysis of shear-driven dynamics, such as the Kelvin–Helmholtz instability (KHI). This study has applications to planetary and terrestrial magnetospheres<sup>22–24</sup> and inner heliospheric observations from Solar Orbiter<sup>25</sup> and Parker Solar Probe (PSP).<sup>26</sup>

## II. BACKGROUND

Much work has been done on linear instability analysis resulting from a shear flow<sup>27,28</sup> and the emphasis is frequently on this small amplitude regime, even though it is well known that shear-driven dynamics quickly approaches a strongly nonlinear regime.<sup>7,29,30</sup> Recent detailed investigation of nonlinear behavior of shear-driven turbulence in kinetic plasma<sup>5</sup> has begun to reveal a rich variety of phenomena, with many questions remaining.

KHI can be understood from Bernoulli's principle, where pressure gradients amplify perturbations across the velocity shear layer, driving the development of vortex structure until vortex stretching causes highly nonlinear behavior and secondary instabilities. Karimabadi *et al.*<sup>5</sup> found that motion associated with coherent structures produces waves that propagate into the ambient plasma. Current sheets also develop, and these are responsible for heating rates greater than those associated with wave damping. However the heating rate estimate in Karimabadi *et al.*<sup>5</sup> is solely based on electromagnetic work. Using the same shear-driven simulation, Wan *et al.*<sup>31</sup> identified intermittency and nonuniform dissipation in the nonlinear regime, but did not explore the time evolution of these characteristics. The present paper aims to expand upon these by using recent developments in kinetic turbulence and dissipation.<sup>32,33</sup>

Prior works correctly describe energy conversion between magnetic and fluid flow as due to electromagnetic work, but they do not completely describe the details of conversion into thermal energy. In plasmas, collisional or collisionless, the total energy can be decomposed into electromagnetic, species fluid flow, and species thermal (random) components where energy transfer occurs between each. The time evolution of the second moment of the Vlasov–Maxwell equations is given by

$$\partial_t E_\alpha^f + \nabla \cdot (E_\alpha^f \mathbf{u}_\alpha + \mathbf{P}_\alpha \cdot \mathbf{u}_\alpha) = (\mathbf{P}_\alpha \cdot \nabla) \cdot \mathbf{u}_\alpha + \mathbf{j}_\alpha \cdot \mathbf{E}, \quad (1)$$

$$\partial_t E_\alpha^{th} + \nabla \cdot (E_\alpha^{th} \mathbf{u}_\alpha + \mathbf{h}_\alpha) = -(\mathbf{P}_\alpha \cdot \nabla) \cdot \mathbf{u}_\alpha, \quad (2)$$

$$\partial_t E^m + \frac{c}{4\pi} \nabla \cdot (\mathbf{E} \times \mathbf{B}) = -\mathbf{j} \cdot \mathbf{E}, \quad (3)$$

where  $\alpha$  denotes species,  $\mathbf{P}_\alpha$  is the pressure tensor,  $\mathbf{h}_\alpha$  is the heat flux tensor,  $\mathbf{j}$  ( $\mathbf{j}_\alpha$ ) is the total (species) current density, and  $E_\alpha^f = \frac{c}{2} \mathbf{u}_\alpha^2$ ,  $E_\alpha^{th} = \frac{m_\alpha}{2} \int (\mathbf{v} - \mathbf{u})^2 f_\alpha(\mathbf{x}, \mathbf{v}, t) d\mathbf{v}$ ,  $E^m = \frac{1}{8\pi} (\mathbf{B}^2 + \mathbf{E}^2)$  are the fluid, thermal, and electromagnetic energies, respectively. In each of these equations, the transport terms inside the divergence operators can be neglected in periodic boundary systems when averaged over the box. It can be observed that the electromagnetic work on the system ( $\mathbf{j}_\alpha \cdot \mathbf{E}$ ) signifies the transfer between electromagnetic and fluid flow energy, and the pressure strain interaction  $-(\mathbf{P}_\alpha \cdot \nabla) \cdot \mathbf{u}_\alpha$  represents conversion between fluid flow and internal energy.<sup>32</sup> We abbreviate pressure strain interaction as  $PS_e$  and  $PS_i$  for electrons and ions, respectively. These energy transfer terms are bidirectional, and are often occurring

at varying spatial scales. Further decomposition into isotropic and anisotropic portions of the pressure strain interaction results in

$$\underbrace{\langle -(\mathbf{P}_\alpha \cdot \nabla) \cdot \mathbf{u}_\alpha \rangle}_{PS_\alpha} = \underbrace{\langle -p_\alpha \nabla \cdot \mathbf{u}_\alpha \rangle}_{p\theta_\alpha} + \underbrace{\langle -\Pi_\alpha : \mathbf{D}_\alpha \rangle}_{PiD_\alpha}, \quad (4)$$

where  $\langle \dots \rangle$  denotes a volume average,  $p$  is the scalar pressure, and  $D_\alpha$  is the deviatoric (traceless) strain tensor, while  $p\theta_\alpha$  and  $PiD_\alpha$  are familiar abbreviations for the pressure dilatation and the remaining “gyroviscous” contribution to the pressure strain. This brief summary (see Yang *et al.*<sup>32</sup>) provides the basis for our analysis below.

The rest of the paper is organized as follows: Sec. III discusses the simulation used along with the normalizations, followed by Sec. IV, which includes the results. Finally, in Sec. V, we present the conclusions and discussions of this study.

## III. SIMULATION

The transition of a shear flow to turbulence is modeled using VPIC,<sup>34</sup> a particle-in-cell (PIC) code that time evolves the Vlasov–Maxwell equations, with fluctuations polarized in three dimensions but varying in the (x,y) plane, and no variation in the  $\hat{z}$  direction. The initial magnetic field is uniform and defined as  $\mathbf{B} = B_0(\sin\theta\hat{y} + \cos\theta\hat{z})$ , where  $B_0$  is the magnetic field intensity. The particles are initially loaded as a drifting Maxwellian with a uniform temperature  $T$  and a nonuniform drift speed of  $U_y = U_0 \tanh(x/L_V)$ , where  $U_0$  is the shear velocity and  $L_V$  is the shear layer half-thickness. To initiate the dynamics, a velocity perturbation is imposed, varying as  $\delta U_y = \delta U_0 \sin(0.5y/L_V) \exp(-x^2/L_V)$ , where  $\delta U_0 = 0.15U_0$ . The initial electric field is defined as  $\mathbf{E} = -(B_z U_0/c) \tanh(x/L_V) \hat{x}$ ; to support this field, a small amount of excess electron density is added, defined as  $n_e(x) = B_z U_0/(4\pi e L_V) \text{sech}^2(x/L_V)$ . The boundaries are periodic along  $\hat{y}$ , but along  $\hat{x}$  the “wall” is conducting for electromagnetic fields and reflecting for particles.

We use normalized PIC units, where mass is normalized to mass of electrons  $m_e$ , charge is normalized to electron charge  $e$ , length is normalized to the electron skin depth  $d_e = c/\Omega_{pe}$ , time is normalized to the inverse of the electron plasma frequency  $\Omega_{pe}^{-1} = (\sqrt{4\pi n_0 e^2/m_e})^{-1}$ , where  $n_0$  is the normalization for number density initially set to be uniform everywhere, and velocity is normalized to the speed of light  $c$ . In addition, the ratio of ion to electron mass  $m_i/m_e$  and the ratio of electron plasma frequency to electron cyclotron frequency  $\Omega_{pe}/\Omega_{ce}$  are set as free parameters that control the ratio of ion to electron skin depth  $d_i/d_e$  and the in-plane magnetic field strength  $B_0$ , respectively.

The simulation is performed in a rectangular box of size  $(L_x, L_y) = (125 \times 250)d_e = (12.5 \times 25)d_i$  with a computational domain of  $1280 \times 2560$  grids, a grid spacing of  $\delta x = 0.09765d_e = 0.8735\lambda_D$ , where  $\lambda_D$  is the electron Debye length, and a time step of  $dt = 2.762 \times 10^{-4} \Omega_{ci}^{-1} = 0.0552 \Omega_{pe}^{-1}$ . The simulation used 200 particles per cell for each species corresponding to a total of  $1.3 \times 10^9$  particles. Among other parameters,  $m_i/m_e = 100$ ,  $\Omega_{pe}/\Omega_{ce} = 2$ ,  $B_0 = 0.5$ ,  $U_0 = 0.025c = 10V_A^*$ , where  $V_A^* = B_0 \sin\theta/\sqrt{4\pi n_0 m_i}$  is the in-plane Alfvén velocity,  $L_V = 10d_e$ ,  $T_i = T_e = 0.0125$ , plasma beta  $\beta = 0.1$ , and  $\theta = 2.86^\circ$ , which means the background magnetic field is mostly out of the plane. The simulation is run for a total time of  $t = 156 \Omega_{ci}^{-1} = 5.7\tau_{nl}$ , where  $\tau_{nl}$  is the global nonlinear time defined as  $\tau_{nl} = L_x/u_{rms}^e$  and  $u_{rms}^e$  is the rms of electron velocity fluctuations.<sup>35</sup>

These initial conditions are similar to those used in Karimabadi *et al.*<sup>5</sup> and Wan *et al.*<sup>31</sup> The main differences in the present paper are (Karimabadi *et al.*<sup>5</sup> values in parentheses) a smaller box size ( $50d_i \times 100d_i$ ), lower resolution ( $\delta x = 0.77\lambda_D$ ), but more particles per cell (150). Note that the in-plane magnetic field has initial energy per unit mass that is 1% of the corresponding value in the velocity field. For presentation, all analyses make use of filtered data (as described below) to avoid effects of discrete particle noise.

#### IV. RESULTS

Figure 1 shows the time evolution of the mean squared current  $\langle j^2 \rangle$  and mean square electron vorticity  $\langle \omega_e^2 \rangle$ . Note that electron vorticity ( $\omega_e = \nabla \times u_e$ ) includes contributions from isolated flow circulation patterns as well as planar shear layers across which electron flow reverses. This simulation begins with a nonzero electron vorticity as a result of the initial large-scale shear layer. The mean square current attains a maximum at  $t\Omega_{ci} = 70$ , often denoted as the time of maximum turbulence, while the mean square electron vorticity continues to increase (roughly linearly) and peaks at  $t\Omega_{ci} = 90$  due to the effect of secondary instabilities in the system. The standard explanation is that reconnection inflows compress field lines and thin the current sheet, thus amplifying the mean square current. The inflow magnetic field interacts with the gradient of the current to produce a torque that amplifies vorticity (see Parashar and Matthaeus<sup>36</sup>). Activity such as stretching and compression of vortices have been identified in other shear layer-driven simulations.<sup>13,37,38</sup>

For the purpose of our study, we divide the time evolution into four distinct phases—I, II, III, and IV ( $t\Omega_{ci} = 41, 70, 90, 150$ , respectively)—that represent the stages of the development to turbulence. Phase I represents the initial nonlinear development of the shear instability; phase II represents amplification of current density during transition to turbulence; phase III represents attainment of peak vorticity during formation of secondary nonlinear instabilities; and phase IV represents the epoch of fully developed turbulence. Phases II and III have also been chosen as they correspond to regimes of large rates of energy transfer into thermal energy.

The top panel of Fig. 2 displays the omnidirectional ion flow energy spectrum (per unit mass), and the bottom panel shows the magnetic energy spectrum as a function of wavenumber  $k$  in different phases of the simulation. A low-pass Fourier filter at  $kd_e = 5$ , indicated by a solid red line, is used in all analyses to reduce particle noise. Initially, both ion flow and electromagnetic energy are confined within

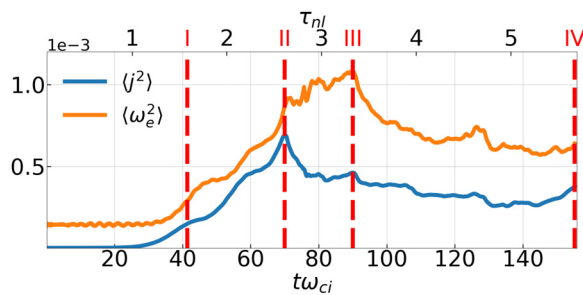


**FIG. 1.** Time evolution of the mean squared current  $\langle j^2 \rangle$  and electron vorticity  $\langle \omega_e^2 \rangle$ . The dashed vertical lines represent the initiation of different phases in the evolution as discussed in the text and indicated by the roman numerals.

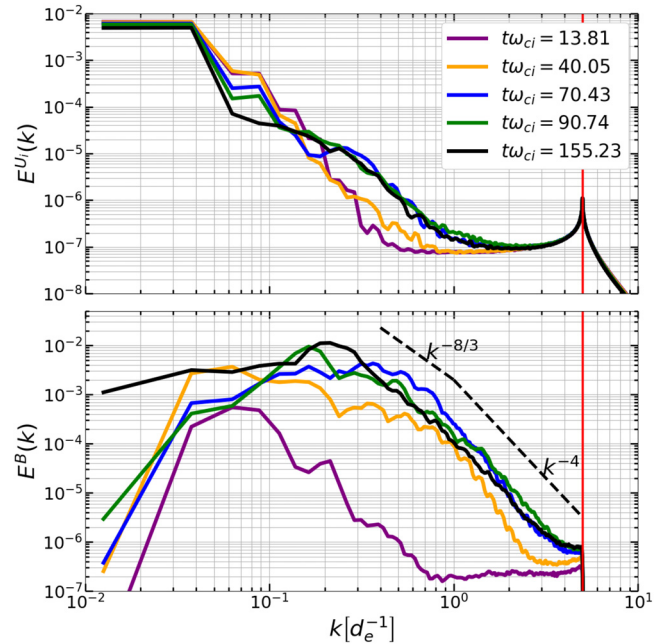


**FIG. 2.** Omnidirectional ion kinetic energy (top) and magnetic energy (bottom) spectrum before, during, and after the transition to the nonlinear regime. Dashed lines of slope  $-8/3$  and  $-4$  are drawn for reference. The red vertical line at  $kd_e = 5$  represents the cutoff for a low-pass Fourier filter performed to eliminate discrete particle noise.

the smaller wavenumber range, but as the system evolves, energy transfers to higher wavenumbers. As a result, the magnetic energy spectrum exhibits a slope of about  $-8/3$  for  $0.4 \leq kd_e \leq 1.2$ . This spectral range is frequently associated with kinetic Alfvén waves (KAWs).<sup>39</sup> Further, as the system reaches phase III, the spectrum exhibits another power law of slope  $-4$  from  $1.2 \leq kd_e \leq 5$ , which remains essentially unchanged until the late stage of the simulation. These findings are consistent with Kelvin–Helmholtz instabilities identified in Earth’s Magnetosphere.<sup>40</sup>

Next, in Fig. 3, we give an overview of the different stages of the simulation and relate these with corresponding energy dissipation proxies, including  $j \cdot E$ ,  $PiD$  for ions and electrons, and  $p\theta$  for ions.  $p\theta$  for electrons is not shown as it does not strongly relate to the characteristic features present in other plotted quantities amid the background noise. The separate phases display the transition to the nonlinear regime resulting from the shear flow dynamics. Energy transfer related to fluid flow and electromagnetic energy ( $j \cdot E$ ) corresponds well with the current structures, while the electron dissipation into internal energy ( $PiD_e$ ) appears to be correlated with electron vortical structures. We revisit this quantitatively below (in Fig. 7).

Phase I displays characteristic “spines,” that is, formations of current sheets on the edge of vortices, which are often the spatial signature resulting from nonlinear roll-ups.<sup>5,41</sup> In this case, electron vorticity also accumulates in a similar spinal pattern. From visual inspection, we find that  $PiD_e$  heats electrons (note density of positive red values) along the spines during this phase. At the same time,  $PiD_i$  has a broad structure with a width of about  $\Delta x = 4d_i$ , where ions are being cooled inside the vortex roll-up, but heated along the spines. However, the



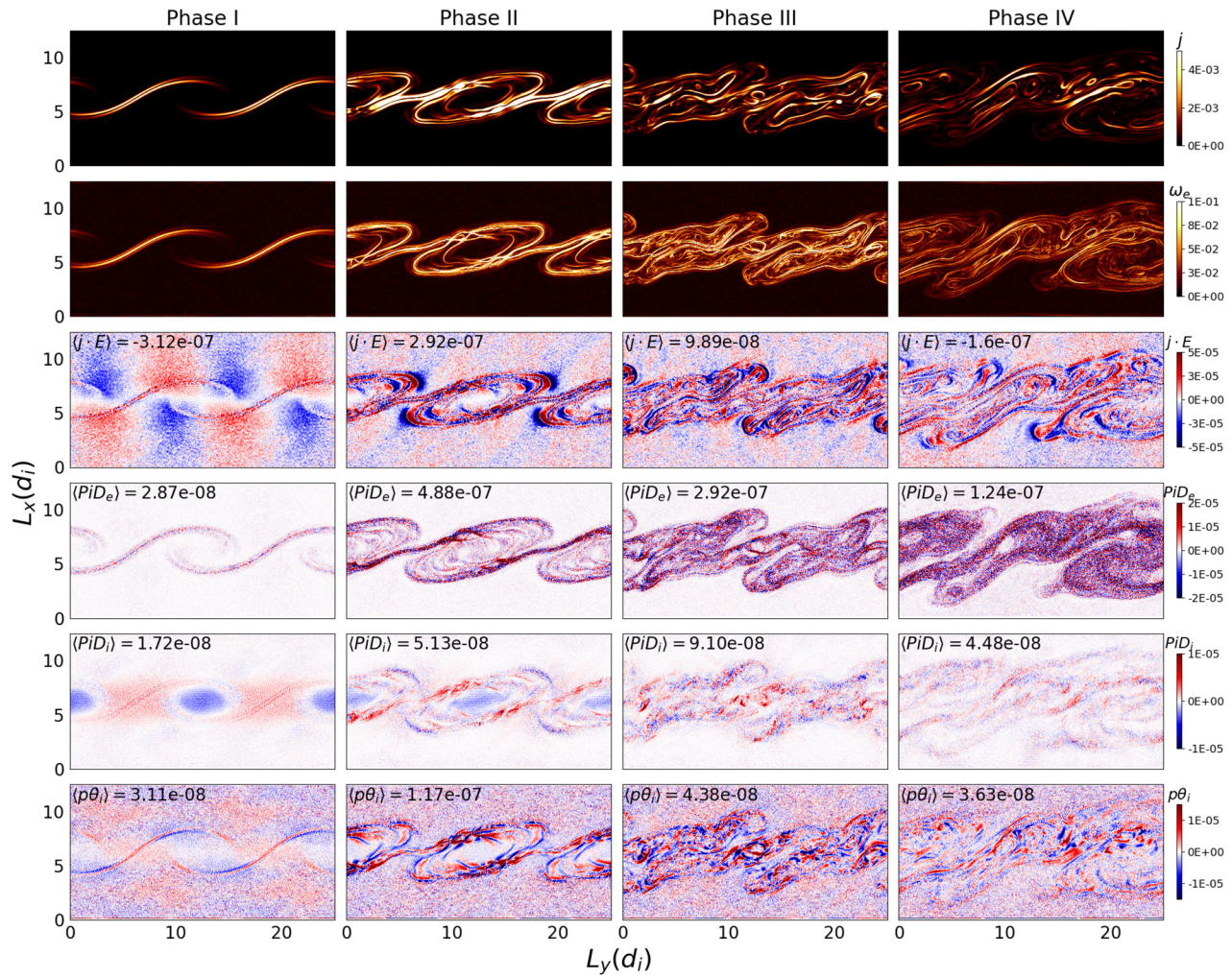


**FIG. 3.** Snapshots of current density ( $j$ ), electron vorticity ( $\omega_e$ ), and energy dissipation related to the development of the shear layer to turbulence. A Fourier filter is performed at  $kd_e = 5$  (see Fig. 2) to reduce noise. Spatial averages of thermal energy dissipation are displayed in the plot.  $j$  is normalized to  $ec/d_e^2$ ,  $\omega_e$  to  $c/d_e$ , and energy transfer components to  $m_e c^3/d_e$ .

heating and cooling sections for ions swap every  $t\Omega_{ci} \approx 1.2$  as shown by the global averages in Fig. 5. The physics behind these oscillations is discussed below.

In Phase II, we view the moment right before reconnection begins to dominate over the initial shear layer. During this phase, the spines are being heated by shear components as indicated in  $PiD_e$  and  $PiD_i$ . This development of reconnection inside vortex roll-ups is consistent with the original descriptions of reconnection resulting from KHI events<sup>37</sup> and recently identified in other PIC simulations.<sup>13</sup> We also see compressive ion heating and cooling along the spines as seen in  $p\theta_i$ . After reconnection occurs, the oscillations of  $PiD_i$  are no longer observed. During phase II, we find that shear heating of electrons is approximately an order of magnitude larger than shear heating of ions. Interestingly, fluid energy conversion into electromagnetic energy ( $j \cdot E$ ) attains its greatest values at the outer edge of the vortices, while

conversion from fluid to thermal energy ( $PiD_e$  and  $PiD_i$ ) occurs along the vortex spines.

In phases III and IV, the dynamics have evidently become more turbulent (see Fig. 1), and the shear flow energy has converted into smaller scale structures as seen in Fig. 3. In phase III, the vortices break into smaller structures and begin to lose their resemblance to the initial roll-ups. Phase IV provides an example of the late stage turbulent regime of plasma KH dynamics, and exhibits multiple small-scale structures most likely due to electron-only reconnection. By this point, we see a wide separation of scales in which the coherent structures in various forms—regions with enhanced current, vorticity, and proxies of dissipation (electromagnetic work and pressure strain interaction)—occupy most of the system. Note that this time frame in phase IV is also used for analysis of late stage decaying turbulence in Figs. 6 and 7.

Throughout this simulation, as seen in Fig. 3, it is apparent that the conversion between electromagnetic and fluid energies occurs on larger scales than the conversion between fluid and thermal energies. For this, note the comparison between  $j \cdot E$  and  $PiD_e$  and, in particular, the finer spatial scales of the latter. While both  $j \cdot E$  and  $PiD_e$  both contain positive and negative points, the areas of the consistently signed patches of points are mostly larger for  $j \cdot E$  than for  $PiD_e$ . This has also been observed and discussed further in other fully developed turbulence simulations analyzed through scale filtering.<sup>9</sup>

To further analyze the evolution of the system, we calculate the changes of the several energy ingredients. Figure 4 displays the changes of energy in different components during the time of the simulation, and this is compared to the time integrated corresponding rates of energy transfer in those components. The initial large reservoir of ion flow energy is converted to other forms of energy throughout the simulation, most significantly to the electron thermal energy. The total energy of the simulation is conserved to within 0.39%, indicating numerical validity of the simulation.

To remove the initial transient fluctuations in the system associated with the numerical setup, we begin the time integration at  $t\Omega_{ci} = 7$ . We find that the comparison of energy dissipation proxies to differential energies agrees well, except for the electron thermal and fluid components. This discrepancy is most likely due to small accumulative relativistic effects and numerical errors. Energy output from ion fluid energy is approximately linearly decreasing after  $t\Omega_{ci} = 45$ . At  $t\Omega_{ci} = 70$ , we clearly see the impacts of reconnection since the magnetic energy begins to decrease, and much of that energy is converted to electron and ion thermal energies. After about  $t\Omega_{ci} = 80$ , the rate of change of magnetic energy is constant on average; however, while both the ion and electron internal energies are increasing linearly in time, the electron heating is about twice as fast as that of ions by the end of the simulation.

Figure 5 displays the spatial average of the decomposed pressure strain interaction as a function of time. Here, we see that the enhanced rates of internal energy production for both ions and electrons are

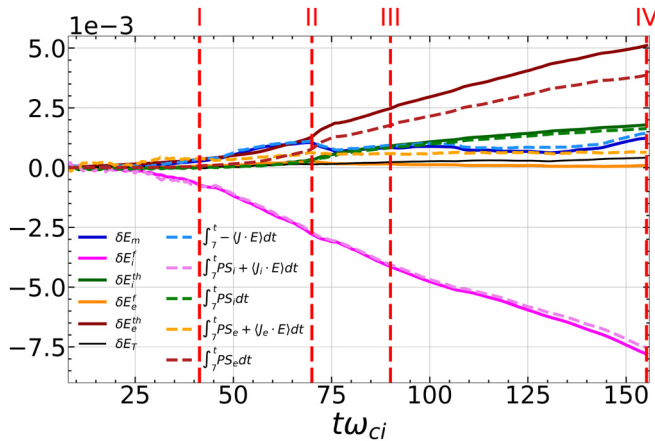


**FIG. 4.** Time evolution of changes in decomposed forms of energies. Here,  $\delta E_m$  (electromagnetic energy),  $\delta E^f$  (flow energy), and  $\delta E^th$  (thermal energy) are shown. These energy changes are compared to the cumulative time integrated energy transfer terms from the moments of the Vlasov–Maxwell system. The subscripts  $i$  and  $e$  represent ions and electrons, respectively.

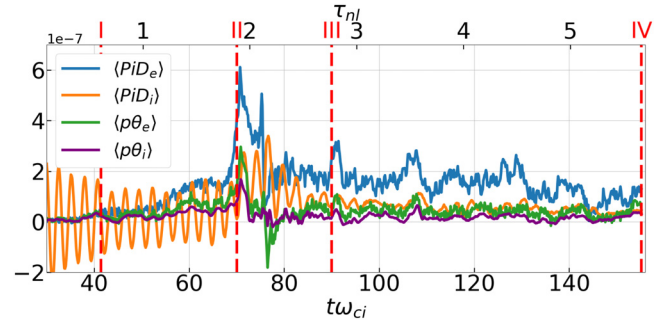


**FIG. 5.** Spatially averaged decomposed pressure strain interaction for ions and electrons. All components of the pressure strain peak close to phase II, where the maximum current density occurs. There is a significant drop at  $t\Omega_{ci} \approx 77$ , indicating a relaxation from the initial reconnection along the spines. There is a second peak in energy dissipation following the point of maximum mean square electron vorticity.

initiated at the onset of phase II and persist thereafter. At  $t\Omega_{ci} \approx 77$ , we notice a significant decrease in the rate of production of electron internal energy, indicating a sharp relaxation once the reconnection energy has dissipated. Prior to this time,  $\langle PiD_i \rangle$  experiences significant oscillations, the largest contribution being from  $PiD_{xy}$  located along the shear layer (not shown). Similar oscillations occurring soon after the initial conditions have been reported previously, for example, in a 3D hybrid simulation of decaying plasma turbulence.<sup>42</sup> The nature of such oscillations has been explored by Cerri *et al.*<sup>43</sup> who attribute such effects as due to an initialization based on MHD, rather than a quieter start based on extended physics such as finite Larmor radius effects. Such simplifications in startup of plasma simulations usually lead to transient effects such as what is seen in the early stages of the present simulation. Beginning after  $t\Omega_{ci} > 70$ , this oscillation dies away and, in phase II, is progressively replaced by the plasma dynamics of physical interest. Finally, after  $t\Omega_{ci} > 90$ , the dynamics in phase III attains a reasonably steady character with regard to the conversion channels into internal energy shown in Fig. 5.

To better understand the structure of dissipation and its development over time, we focus on later dynamical stages (from II to IV), and calculate energy dissipation conditioned on thresholds of electron vorticity and current density. A complementary quantity is the area filling fraction of locations with electron vorticity or current exceeding specified thresholds. This fractional measure provides evidence of the intensity of energy conversion in relation to vortical vs current structures. These quantities are then compared during the turbulent evolution, in particular in phases II and IV. We recall that the former represents the time of maximum mean square current, and the latter the phase of fully developed turbulent decay. We focus on the electron electromagnetic work and electron  $PiD$  since the plasma dynamics are mostly dominated by electrons.

The average of quantity  $f$  conditioned on a threshold on  $n$  is performed by computing

$$F(f|n) = \frac{\sum' f}{\sum' 1}, \quad (5)$$

where  $f$  is a general quantity, and  $\sum'$  is a sum over points where  $n$ , meaning either  $j/j_{rms}$  or  $\omega_e/\omega_e^{rms}$ , exceeds a given value. The area filling



fraction is  $F(1|n)$ , that is the fraction of the area in which the normalized quantity  $f/f_{rms}$  exceeds  $n$ .

Figure 6 shows the conditional averages of electron  $PiD$  and electromagnetic work ( $j_e \cdot E$ ), along with the fractional area (green squares) in which normalized current density ( $j/j_{rms}$ ) and normalized electron vorticity ( $\omega_e/\omega_e^{rms}$ ) exceed  $n$ . We display this at two times corresponding to phases II and IV.

During phase II, the fractional rate of energy conversion from flow to thermal ( $PiD_e$ ) is greater than the fractional rate of conversion of electromagnetic to flow ( $j_e \cdot E$ ) at all values of the condition  $\omega_e/\omega_e^{rms}$ . However, this is not the case for the same quantities conditioned on  $j/j_{rms}$ . During the late phase (IV) with a threshold on vorticity, the energy conversion fraction from electromagnetic to electron flow ( $j_e \cdot E$ ) is greater than unity up to condition  $\omega_e/\omega_e^{rms} = 0.5$ . Following this point, the fractional energy falls until  $\omega_e/\omega_e^{rms} = 1.5$ . For higher thresholds, the electromagnetic work falls similarly to phase II. Interestingly, a contrasting behavior is seen in the fractional electromagnetic work conditioned on current, where it is greater than 1 up to  $j/j_{rms} = 1.75$ . Note that the fractional energy transfer terms are able to exceed unity for quantities that are not positive definite. However, by definition, the values with no threshold ( $f/f_{rms} = 0$ ) must equal one.

At all times, fractional energy transfer is larger than fractional area, except for a few points of  $j_e \cdot E$  with a threshold on vorticity. The area measured in Fig. 6 shows that regions of stronger electron current density and electron vorticity occupy smaller regions, but make significant, disproportionate contributions to the net conversion of energy, which is consistent with Wan *et al.*<sup>31</sup> This is a reflection of the intermittency of energy conversion in shear-driven plasma turbulence.

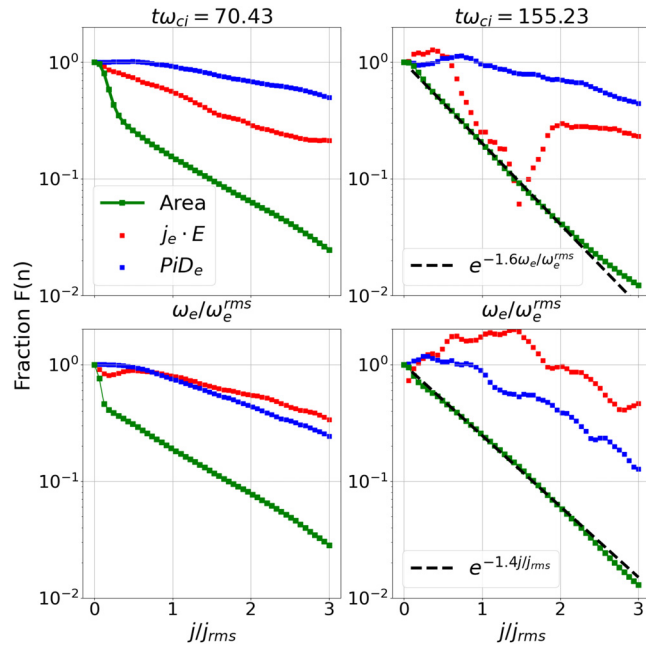


**FIG. 6.** Fractional area and energy dissipation conditionally averaged on (top)  $\omega_e/\omega_e^{rms}$  and (bottom)  $j/j_{rms}$  threshold at (left)  $t\Omega_{ci} = 70.43$  and (right)  $t\Omega_{ci} = 155.23$ .

For both vorticity and current, the area filling fractions have large initial drops until about 0.25, which saturates to an exponentially decreasing function in phase IV. At the late phase, the area fraction for vorticity and current follow a similar exponentially decreasing function. This implies that the areas with region of higher vorticity and current fall at roughly the same rates and thus have similar distribution functions. This finding is analogous to the findings of Schekochihin *et al.*,<sup>44</sup> which show that intermittency of normalized magnetic field strength is lower in the saturated stage.

The rates of production of internal (thermal) energy for each species are accurately accounted for by the respective pressure strain interactions.<sup>9</sup> The averages of these heating rates ( $PiD_e$  and  $PiD_i$ ), conditioned on local intensities of vorticity, traceless strain, and current, are shown in Fig. 7. It is expected that eventually the full reservoir of initial flow shear energy will be converted to heat, as this simulation is undriven. Evaluating the correlation of heating with spatial structures is an important feature of the turbulence as energy transfer into heat is a dominant feature as displayed in Fig. 4. Using conditional averaging, previous studies<sup>36,45</sup> have examined correlations between electron and ion pressure strain and the second tensor invariants of vorticity, traceless strain, and current density, defined as

$$Q_\omega^z = \frac{\omega_z^2}{4\langle\omega_z^2\rangle}; \quad Q_D^z = \frac{D_{ij}^z D_{ij}^z}{4\langle D_{ij}^z D_{ij}^z \rangle}; \quad Q_j = \frac{j^2}{4\langle j^2 \rangle}. \quad (6)$$

Prior works have studied these correlations for Alfvénic turbulence and only at a single time. Here, we extend that investigation to the shear-driven case, and at two phases of temporal development. We require the conditional averages to contain at least  $10^3$  points for electrons and  $10^2$  for ions at the largest shown threshold.

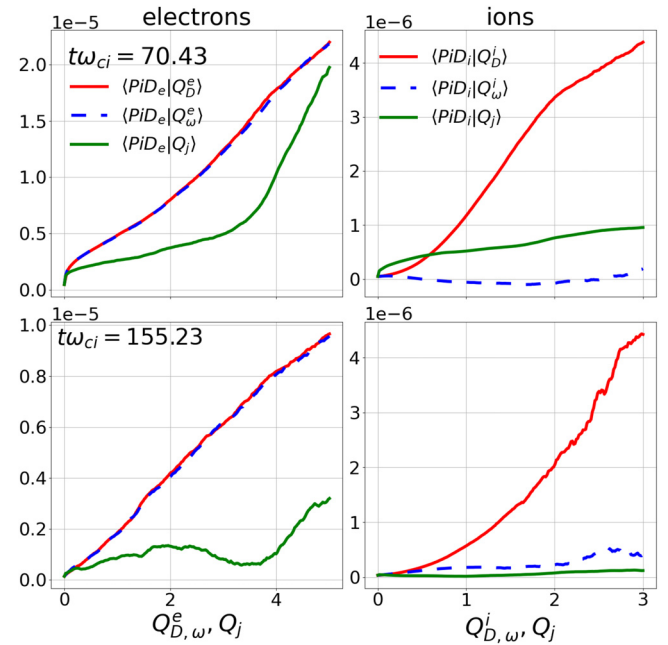


**FIG. 7.** Averaged electron (left) and ion (right) pressure strain interaction conditional on second tensor invariants associated with strain  $Q_D^z$ , vorticity  $Q_\omega^z$ , and current  $Q_j$  at same times in Fig. 6.

Figure 7 shows these several conditional averages of ion and electron  $PiD$  at the same times shown in Fig. 6. In the later stages, the behavior of the conditional averages follows similar trends to what has been found previously.<sup>36,45</sup> For ions, thermal dissipation is related to strain and is consistent through time. For electrons, we find that the electron  $PiD$  is better correlated with vorticity and traceless strain, rather than current density. The electron  $PiD$  at maximum turbulence appears to have correlations of varying degree with all quantities. On average,  $\langle PiD_e | Q_D^e \rangle$  and  $\langle PiD_e | Q_{\omega}^e \rangle$  indicate the strongest correlations that increase nearly linearly for strong strain and vorticity. The near equality of these two measures indicates that  $Q_D^e \sim Q_{\omega}^e$ , thus suggesting that electron dissipation occurs preferentially in sheet-like vorticity structures (shear layers), rather than in isolated circulating vortices. The correlation with current is not as strong, and may be a result of the broad current sheets overlapping nearby vortices<sup>36</sup> as suggested in Fig. 3. This is to be expected during a large reconnection event. At later stages, the  $PiD_e$  correlation with current is much weaker, leaving mainly correlations with  $Q_D^e$  and  $Q_{\omega}^e$ . We note that, for ions, in contrast to the electrons, the conversion to internal energy is much more strongly correlated with rate of strain than it is for vorticity. This implies that the characteristic intense dynamically produced structures in the proton fluid are not mainly sheet-like as they are for the electron fluid. The ion vorticity is of course a dominant factor in the initial data that drive the nonlinear Kelvin–Helmholtz dynamics.

## V. DISCUSSION AND CONCLUSION

Turbulence in MHD, and even more so in collisionless plasma, is more complex than hydrodynamics, and a full classification of different types of plasma turbulence remains an ongoing area of research. Even in MHD, there are potentially many classes of behavior, so as to make the idea of universality elusive. Sorting cases of interest according to a few controlling features such as the energy source (or mean magnetic field strength, plasma beta, level of compressibility, etc.) remains a worthwhile approach. Here, we examined the case in which the turbulence is driven by nonlinear instability of an initial velocity shear. This contrasts with the well-studied case driven by initially strong magnetic shear that is magnetic reconnection in the presence of turbulence.<sup>46–48</sup> The present interest in examining details of energy conversion in shear-driven kinetic turbulence may be viewed as a follow-up to the work of Karimabadi *et al.*,<sup>5</sup> which examined many details of a system very similar to that examined here. Our motivation has been to provide a more in-depth treatment of energy conversion for the shear-driven system, especially in view of recent theoretical developments.<sup>9,11,32</sup> A particular focus here has been on quantifying channels of energy conversion between electromagnetic fields, and species-dependent plasma flows and internal energies.

The specific emphasis here has been the decomposition of energy transfer and conversion throughout the dynamical development. We presented details of the species-dependent pressure strain interaction and electromagnetic work<sup>49</sup> during the transition to turbulence and in the fully developed phase. Conditional averaging of the dissipation proxies provides insight into the development intermittent energy transfer. We also identify correlations of energy conversion with coherent structures, finding that the associations are similar to those found in decaying turbulent simulations beginning with equipartitioned velocity and magnetic field perturbations.<sup>32</sup> This suggests that the turbulence generation from Alfvénic fluctuations is mostly contributed by shear flow energy transfer, and reaches a correlation equilibrium with

vorticity and strain for electrons, and solely strain for ions. Further, we have identified the role of the nonlinear structures in the energy dissipation process that can be used in comparison with recent spacecraft observations. To this point, Parker Solar Probe (PSP)<sup>26</sup> and Solar Orbiter data<sup>25</sup> have recently shown evidence of energy transfer due to linear or nonlinear Kelvin–Helmholtz dynamics (see also Ruffolo *et al.*<sup>50</sup>). This is particularly applicable as PSP has only recently probed the sub-Alfvénic solar wind, which is thought to suppress KHI, although the finding of significant deviations from WKB theory suggests input by large-scale coronal shear flows.<sup>51</sup>

Most recently,  $PiD$  is shown to have a compressive element embedded within it.<sup>52</sup> However, examining the role of compressive  $PiD$  in shear turbulence is left for a future study. We note the dissipation mechanisms such as those studied here have been shown to have dependency on the proton–electron mass ratio,<sup>53</sup> which tend to asymptote around  $m_i/m_e = 250$ . While increasing the mass ratio, and therefore the scale separation, would provide greater accuracy, it is unlikely to qualitatively alter the underlying physics discussed in our study. Further, other studies have derived the kinetic processes associated with the pressure strain interaction<sup>54</sup> in standing Langmuir and traveling Alfvén waves. Such analysis may be illuminating in the present context to reveal dynamical properties in the velocity space.

While this study reveals nonlinear features of shear-driven turbulence in an idealized setting, changes to the computational scope and details might be necessary to accurately depict the complexities of the solar wind. For example, the physical dimensions used in this study, such as box size and shear flow boundary layer, are smaller (measured in  $d_i$ ) than physical dimensions inferred from the Magnetosphere Multiscale (MMS) measurements, with the boundary layer thickness at the flanks measuring approximately  $11\text{--}15\,d_i$ .<sup>55</sup> Such numerical compromises (see Karimabadi *et al.*,<sup>5</sup> Ahmadi *et al.*<sup>13</sup>) are often made to reduce the computational cost while adequately maintaining kinetic-scale resolution. Furthermore, this simple initial value problem does not include additional sources of turbulent fluctuations occurring throughout the system. In future work, we will explore how these fluctuations impact the energy cascade as well as the shear layer development. Furthermore, a parameter study that varies plasma  $\beta$  will provide details on the differences of shear layers in the solar corona vs the Earth’s magnetosphere.

## ACKNOWLEDGMENTS

This research is supported part by LANL through its Center for Space and Earth Science (CSES), by a Delaware Space Grant Graduate Fellowship (80NSSC20M0045), by NASA under the IMAP mission theory project at UD (Princeton subcontract SUB0000317), the MMS Theory and Modeling team (Grant No. 80NSSC19K0565), and by the National Science Foundation Solar Terrestrial Program Grant No. PHYS-2108834 at the University of Delaware. CSES is funded by LANL’s Laboratory Directed Research and Development (LDRD) program under Project No. 20240477CR. F.P. acknowledges support from the Research Foundation—Flanders (FWO) Junior research project on fundamental research G020224N.

## AUTHOR DECLARATIONS

### Conflict of Interest

The authors have no conflicts to disclose.



## Author Contributions

**J. Goodwill:** Investigation (equal); Methodology (equal); Resources (equal); Software (equal); Visualization (equal); Writing – original draft (equal). **S. Adhikari:** Resources (equal); Software (equal); Supervision (equal); Writing – review & editing (equal). **X. Li:** Resources (equal); Software (equal). **F. Pucci:** Investigation (equal); Methodology (equal). **Y. Yang:** Conceptualization (equal); Methodology (equal); Software (equal); Visualization (equal). **F. Guo:** Conceptualization (equal); Funding acquisition (equal); Investigation (equal); Software (equal); Supervision (equal); Visualization (equal); Writing – original draft (equal). **W. H. Matthaeus:** Conceptualization (equal); Funding acquisition (equal); Investigation (equal); Methodology (equal); Project administration (equal); Resources (equal); Software (equal); Supervision (equal); Validation (equal); Visualization (equal); Writing – original draft (equal); Writing – review & editing (equal).

## DATA AVAILABILITY

The data that support the findings of this study are available from the corresponding author upon reasonable request.

## REFERENCES

- <sup>1</sup>S. Chandrasekhar, “On the stability of the simplest solution of the equations of hydromagnetics,” *Proc. Natl. Acad. Sci. U. S. A.* **42**, 273–276 (1956).
- <sup>2</sup>D. A. Roberts, M. L. Goldstein, W. H. Matthaeus, and S. Ghosh, “Velocity shear generation of solar wind turbulence,” *J. Geophys. Res.* **97**, 17115–17130, <https://doi.org/10.1029/92JA01144> (1992).
- <sup>3</sup>K. T. Osman, W. H. Matthaeus, J. T. Gosling, A. Greco, S. Servidio, B. Hnat, S. C. Chapman, and T. D. Phan, “Magnetic reconnection and intermittent turbulence in the solar wind,” *Phys. Rev. Lett.* **112**, 215002 (2014).
- <sup>4</sup>P. L. Pritchett, “Simulation of collisionless electrostatic velocity-shear-driven instabilities,” *Phys. Fluids B* **5**, 3770–3778 (1993).
- <sup>5</sup>H. Karimabadi, V. Roytershteyn, M. Wan, W. H. Matthaeus, W. Daughton, P. Wu, M. Shay, B. Loring, J. Borovsky, E. Leonardis, S. C. Chapman, and T. K. Nakamura, “Coherent structures, intermittent turbulence, and dissipation in high-temperature plasmas,” *Phys. Plasmas* **20**, 012303 (2013).
- <sup>6</sup>T. K. M. Nakamura, H. Hasegawa, W. Daughton, S. Eriksson, W. Y. Li, and R. Nakamura, “Turbulent mass transfer caused by vortex induced reconnection in collisionless magnetospheric plasmas,” *Nat. Commun.* **8**, 1582 (2017).
- <sup>7</sup>A. Malagoli, G. Bodo, and R. Rosner, “On the nonlinear evolution of magnetohydrodynamic Kelvin-Helmholtz instabilities,” *Astrophys. J.* **456**, 708 (1996).
- <sup>8</sup>S. Landi, P. Hellinger, and M. Velli, “Heliospheric magnetic field polarity inversions driven by radial velocity field structures,” *Geophys. Res. Lett.* **33**, 14101, <https://doi.org/10.1029/2006GL026308> (2006).
- <sup>9</sup>Y. Yang, W. H. Matthaeus, S. Roy, V. Roytershteyn, T. N. Parashar, R. Bandyopadhyay, and M. Wan, “Pressure-strain interaction as the energy dissipation estimate in collisionless plasma,” *Astrophys. J.* **929**, 142 (2022).
- <sup>10</sup>M. H. Barbhuiya and P. A. Cassak, “Pressure-strain interaction. III. Particle-in-cell simulations of magnetic reconnection,” *Phys. Plasmas* **29**, 122308 (2022).
- <sup>11</sup>O. Pezzi, H. Liang, J. L. Juno, P. A. Cassak, C. L. Vásconez, L. Sorriso-Valvo, D. Perrone, S. Servidio, V. Roytershteyn, J. M. TenBarge, and W. H. Matthaeus, “Dissipation measures in weakly collisional plasmas,” *Mon. Not. R. Astron. Soc.* **505**, 4857–4873 (2021).
- <sup>12</sup>S. Adhikari, M. A. Shay, T. N. Parashar, P. S. Pyakurel, W. H. Matthaeus, D. Godzieba, J. E. Stawarz, J. P. Eastwood, and J. T. Dahlin, “Reconnection from a turbulence perspective,” *Phys. Plasmas* **27**, 042305 (2020).
- <sup>13</sup>N. Ahmadi, F. D. Wilder, R. E. Ergun, D. Newman, Y. Qi, K. Germaschewski, S. Eriksson, A. Chasapis, and S. Elkington, “Reconnection signatures in Kelvin-Helmholtz instability evolution in 2D PIC simulations,” *Phys. Plasmas* **32**, 022104 (2025).
- <sup>14</sup>A. N. Kolmogorov, “A refinement of previous hypotheses concerning the local structure of turbulence in a viscous incompressible fluid at high Reynolds number,” *J. Fluid Mech.* **13**, 82–85 (1962).
- <sup>15</sup>A. N. Kolmogorov, “The local structure of turbulence in incompressible viscous fluid for very large Reynolds numbers,” *Proc. R. Soc. London, Ser. A* **434**, 9–13 (1991).
- <sup>16</sup>U. Frisch, *Turbulence: The Legacy of an Kolmogorov* (Cambridge University Press, 1995).
- <sup>17</sup>P. J. Coleman, “Dissipation in the solar-wind plasma,” *Astrophys. J.* **153**, 371 (1968).
- <sup>18</sup>A. Chasapis, W. H. Matthaeus, R. Bandyopadhyay, R. Chhiber, N. Ahmadi, R. E. Ergun, C. T. Russell, R. J. Strangeway, B. L. Giles, D. J. Gershman, C. J. Pollock, and J. L. Burch, “Scaling and anisotropy of solar wind turbulence at kinetic scales during the MMS turbulence campaign,” *Astrophys. J.* **903**, 127 (2020).
- <sup>19</sup>R. Bruno and V. Carbone, “The solar wind as a turbulence laboratory,” *Living Rev. Sol. Phys.* **10**, 2 (2013).
- <sup>20</sup>J. Birn and M. Hesse, “Geospace Environment Modeling (GEM) magnetic reconnection challenge: Resistive tearing, anisotropic pressure and Hall effects,” *J. Geophys. Res.* **106**, 3737–3750, <https://doi.org/10.1029/1999JA001001> (2001).
- <sup>21</sup>H. Aluie and G. L. Eyink, “Scale locality of magnetohydrodynamic turbulence,” *Phys. Rev. Lett.* **104**, 081101 (2010).
- <sup>22</sup>J. E. Stawarz, S. Eriksson, F. D. Wilder, R. E. Ergun, S. J. Schwartz, A. Pouquet, J. L. Burch, B. L. Giles, Y. Khotyaintsev, O. L. Contel, P. A. Lindqvist, W. Magnes, C. J. Pollock, C. T. Russell, R. J. Strangeway, R. B. Torbert, L. A. Avanov, J. C. Dorelli, J. P. Eastwood, D. J. Gershman, K. A. Goodrich, D. M. Malaspina, G. T. Marklund, L. Mirioni, and A. P. Sturmer, “Observations of turbulence in a Kelvin-Helmholtz event on 8 September 2015 by the magnetospheric multiscale mission,” *J. Geophys. Res.* **121**, 11,021–11,034, <https://doi.org/10.1002/2016JA023458> (2016).
- <sup>23</sup>A. Masson and K. Nykyri, “Kelvin-Helmholtz instability: Lessons learned and ways forward,” *Space Sci. Rev.* **214**, 71 (2018).
- <sup>24</sup>R. C. Rice, K. Nykyri, X. Ma, and B. L. Burkholder, “Characteristics of Kelvin-Helmholtz waves as observed by the MMS from September 2015 to March 2020,” *J. Geophys. Res.* **127**, e2021JA029685, <https://doi.org/10.1029/2021JA029685> (2022).
- <sup>25</sup>R. Kieokaew, B. Lavraud, Y. Yang, W. H. Matthaeus, D. Ruffolo, J. E. Stawarz, S. Aizawa, C. Foullon, V. Génot, R. F. Pinto, N. Fargette, P. Louarn, A. Rouillard, A. Fedorov, E. Penou, C. J. Owen, T. S. Horbury, H. O’Brien, V. Evans, and V. Angelini, “Solar orbiter observations of the Kelvin-Helmholtz waves in the solar wind,” *Astron. Astrophys.* **656**, A12 (2021).
- <sup>26</sup>E. Pauris, G. Stenborg, M. G. Linton, A. Vourlidas, R. A. Howard, and N. E. Raouafi, “First direct imaging of a Kelvin-Helmholtz instability by PSP/WISPR,” *Astrophys. J.* **964**, 139 (2024).
- <sup>27</sup>A. Miura and P. L. Pritchett, “Nonlocal stability analysis of the MHD Kelvin-Helmholtz instability in a compressible plasma,” *J. Geophys. Res.* **87**, 7431–7444, <https://doi.org/10.1029/JA087iA09p07431> (1982).
- <sup>28</sup>A. Miura, “Kelvin-Helmholtz instability at the magnetospheric boundary: Dependence on the magnetosheath sonic Mach number,” *J. Geophys. Res.* **97**, 10655–10675, <https://doi.org/10.1029/92JA00791> (1992).
- <sup>29</sup>S. A. Orszag and A. T. Patera, “Secondary instability of wall-bounded shear flows,” *J. Fluid Mech.* **128**, 347–385 (1983).
- <sup>30</sup>M. L. Goldstein, D. A. Roberts, and W. H. Matthaeus, “Numerical simulation of interplanetary and magnetospheric phenomena: The Kelvin-Helmholtz instability,” *Sol. Syst. Plasma Phys.* **54**, 113–125 (1989).
- <sup>31</sup>M. Wan, W. H. Matthaeus, H. Karimabadi, V. Roytershteyn, M. Shay, P. Wu, W. Daughton, B. Loring, and S. C. Chapman, “Intermittent dissipation at kinetic scales in collisionless plasma turbulence,” *Phys. Rev. Lett.* **109**, 195001 (2012).
- <sup>32</sup>Y. Yang, W. H. Matthaeus, and T. N. Parashar, “Energy transfer, pressure tensor, and heating of kinetic plasma,” *Phys. Plasmas* **24**, 072306 (2017).
- <sup>33</sup>W. H. Matthaeus, Y. Yang, M. Wan, T. N. Parashar, R. Bandyopadhyay, A. Chasapis, O. Pezzi, and F. Valentini, “Pathways to dissipation in weakly collisional plasmas,” *Astrophys. J.* **891**, 101 (2020).
- <sup>34</sup>K. J. Bowers, B. J. Albright, B. Bergen, L. Yin, K. J. Barker, and D. J. Kerbyson, “0.374 pflop/s trillion-particle kinetic modeling of laser plasma interaction on

- Roadrunner,” in *SC'08: Proceedings of the 2008 ACM/IEEE Conference on Supercomputing* (IEEE, 2008).
- <sup>35</sup>W. H. Matthaeus, S. Oughton, K. T. Osman, S. Servidio, M. Wan, S. P. Gary, M. A. Shay, F. Valentini, V. Roytershteyn, H. Karimabadi, and S. C. Chapman, “Nonlinear and linear timescales near kinetic scales in solar wind turbulence,” *Astrophys. J.* **790**, 155 (2014).
  - <sup>36</sup>T. N. Parashar and W. H. Matthaeus, “Proximity of current and vortex structures: Effects on collisionless plasma heating,” *Astrophys. J.* **832**, 57 (2016).
  - <sup>37</sup>K. Nykyri and A. Otto, “Plasma transport at the magnetospheric boundary due to reconnection in Kelvin-Helmholtz vortices,” *Geophys. Res. Lett.* **28**, 3565–3568, <https://doi.org/10.1029/2001GL013239> (2001).
  - <sup>38</sup>W. H. Matthaeus, “Reconnection in two dimensions: Localization of vorticity and current near magnetic X-points,” *Geophys. Res. Lett.* **9**, 660–663, <https://doi.org/10.1029/GL009i006p00660> (1982).
  - <sup>39</sup>F. Sahraoui, M. L. Goldstein, G. Belmont, P. Canu, and L. Rezeau, “Three dimensional anisotropic  $k$  spectra of turbulence at subproton scales in the solar wind,” *Phys. Rev. Lett.* **105**, 131101 (2010).
  - <sup>40</sup>H. Hasegawa, T. K. Nakamura, D. J. Gershman, Y. Nariyuki, A. F. Viñas, B. L. Giles, B. Lavraud, C. T. Russell, Y. V. Khotyaintsev, R. E. Ergun, and Y. Saito, “Generation of turbulence in Kelvin-Helmholtz vortices at the Earth’s magnetopause: Magnetospheric multiscale observations,” *J. Geophys. Res.* **125**, e2019JA027595, <https://doi.org/10.1029/2019JA027595> (2020).
  - <sup>41</sup>J. R. Johnson, S. Wing, and P. A. Delamere, “Kelvin-Helmholtz instability in planetary magnetospheres,” *Space Sci. Rev.* **184**, 1–31 (2014).
  - <sup>42</sup>P. Hellinger, A. Verdini, V. Montagud-Camps, L. Franci, E. Papini, L. Matteini, and S. Landi, “Anisotropy of plasma turbulence at ion scales: Hall and pressure-strain effects,” *Astron. Astrophys.* **684**, A120 (2024).
  - <sup>43</sup>S. S. Cerri, P. Henri, F. Califano, D. D. Sarto, M. Faganello, and F. Pegoraro, “Extended fluid models: Pressure tensor effects and equilibria,” *Phys. Plasmas* **20**, 112112 (2013).
  - <sup>44</sup>A. A. Schekochihin, J. L. Maron, S. C. Cowley, and J. C. McWilliams, “The small-scale structure of magnetohydrodynamic turbulence with large magnetic Prandtl numbers,” *Astrophys. J.* **576**, 806–813 (2002).
  - <sup>45</sup>Y. Yang, W. H. Matthaeus, T. N. Parashar, P. Wu, M. Wan, Y. Shi, S. Chen, V. Roytershteyn, and W. Daughton, “Energy transfer channels and turbulence cascade in Vlasov-Maxwell turbulence,” *Phys. Rev. E* **95**, 061201 (2017).
  - <sup>46</sup>W. H. Matthaeus and S. L. Lamkin, “Turbulent magnetic reconnection,” *Phys. Fluids* **29**, 2513 (1986).
  - <sup>47</sup>S. Adhikari, T. N. Parashar, M. A. Shay, W. H. Matthaeus, P. S. Pyakurel, S. Fordin, J. E. Stawarz, and J. P. Eastwood, “Energy transfer in reconnection and turbulence,” *Phys. Rev. E* **104**, 065206 (2021).
  - <sup>48</sup>S. Adhikari, M. A. Shay, T. N. Parashar, W. H. Matthaeus, P. S. Pyakurel, J. E. Stawarz, and J. P. Eastwood, “Effect of a guide field on the turbulence like properties of magnetic reconnection,” *Phys. Plasmas* **30**, 082904 (2023).
  - <sup>49</sup>Y. Yang, S. Adhikari, and W. H. Matthaeus, “Electron dissipation and electromagnetic work,” *J. Geophys. Res.* **129**, e2024JA033105, <https://doi.org/10.1029/2024JA033105> (2024).
  - <sup>50</sup>D. Ruffolo, W. H. Matthaeus, R. Chhiber, A. V. Usmanov, Y. Yang, R. Bandyopadhyay, T. N. Parashar, M. L. Goldstein, C. E. DeForest, M. Wan, A. Chasapis, B. A. Maruca, M. Velli, and J. C. Kasper, “Shear-driven transition to isotropically turbulent solar wind outside the Alfvén critical zone,” *Astrophys. J.* **902**, 94 (2020).
  - <sup>51</sup>D. Ruffolo, P. Thepthong, P. Pongkitiwanichakul, S. Roy, F. Pecora, R. Bandyopadhyay, R. Chhiber, A. V. Usmanov, M. Stevens, S. Badman, O. Romeo, J. Wang, J. Goodwill, M. L. Goldstein, and W. H. Matthaeus, “Observed fluctuation enhancement and departure from WKB theory in sub-Alfvénic solar wind,” *Astrophys. J. Lett.* **977**, L19 (2024).
  - <sup>52</sup>S. Adhikari, Y. Yang, and W. H. Matthaeus, “Revisiting compressible and incompressible pressure-strain interaction in kinetic plasma turbulence,” *arXiv:2503.11825* (2025) [physics.plasm-ph].
  - <sup>53</sup>J. Edyvean, T. N. Parashar, T. Simpson, J. Juno, G. L. Delzanno, F. Guo, O. Koshkarov, W. H. Matthaeus, M. Shay, and Y. Yang, “Scale separation effects on simulations of plasma turbulence,” *Astrophys. J.* **972**, 173 (2024).
  - <sup>54</sup>S. A. Conley, J. Juno, J. M. TenBarge, M. H. Barbhuiya, P. A. Cassak, G. G. Howes, and E. Lichko, “The kinetic analog of the pressure-strain interaction,” *Phys. Plasma* **31**, 122117 (2024).
  - <sup>55</sup>S. Haaland, G. Paschmann, M. Øieroset, T. Phan, H. Hasegawa, S. A. Fuselier, V. Constantinescu, S. Eriksson, K. J. Trattner, S. Fadanelli, P. Tenfjord, B. Lavraud, C. Norgren, J. P. Eastwood, H. Hietala, and J. Burch, “Characteristics of the flank magnetopause: MMS results,” *J. Geophys. Res.* **125**, e2019JA027623, <https://doi.org/10.1029/2019JA027623> (2020).